Q. J. R. Meteorol. Soc. (2004), **130**, pp. 3297–3321 doi: 10.1256/qj.03.128

Numerical simulation of the diurnal cycle of marine stratocumulus during FIRE—An LES and SCM modelling study

By ANDREAS CHLOND*, FRANK MÜLLER and IGOR SEDNEV
Max-Planck-Institut für Meteorologie, Hamburg, Germany

(Received 23 July 2003; revised 16 April 2004)

SUMMARY

As part of the European Project on Cloud Systems in Climate Models (EUROCS), the stratocumulus-topped boundary layer has been simulated using the Max Planck Institute Large-Eddy Simulation (LES) model and the European Centre Hamburg Version Single Column Model (ECHAM–SCM). We have addressed the full diurnal cycle of stratocumulus off the coast of California based on observations of the First International Satellite Cloud Climatology Project Regional Experiment (FIRE). The results of the LES model demonstrate that the model is capable of reproducing the observed diurnal cycle of the boundary-layer structure reasonably well. In particular, the LES model reproduces the distinct diurnal variation in liquid-water path and of turbulence profiles due to the forcing imposed by the short-wave heating of the cloud layer. In addition, we have examined the sensitivity of our LES results with respect to the assumed values of various external environmental conditions. We found that the largest contribution to the variance of the LES-derived data products is due to the uncertainties in the cloud-top jumps of liquid-water potential temperature and total-water mixing ratio and to the net radiative forcing.

To evaluate the quality of the representation of stratocumulus in a general circulation model, results from the standard ECHAM–SCM are contrasted with diagnostics from LES simulations. Results of the standard ECHAM–SCM reveal the following deficiencies: values of the liquid-water path are too low, and unrealistically large levels of turbulent kinetic energy within the cloud layer are due to a numerical instability arising from a decoupling of radiative and diffusive processes. Based on these findings, the SCM has been revised. The modifications include the vertical advection scheme, the numerical treatment of diffusion and radiation, and the combination of the 1.5-order turbulent closure model with an explicit entrainment closure at the boundary-layer top in combination with a front tracking/capturing method. It is demonstrated that, with these modifications, the revised SCM produces a fair simulation of the diurnal cycle of the stratocumulus-topped boundary layer which is significantly improved compared to the one performed with the standard SCM.

KEYWORDS: Boundary-layer clouds Parametrization

1. INTRODUCTION

The European Project on Cloud Systems in Climate Models (EUROCS) aimed to improve the treatment of cloud systems in global and regional climate models. Clouds probably remain the largest source of uncertainty affecting evaluations of climate change in response to anthropogenic influence. That explains for a large part why the range of simulated temperature changes (1.4 to 5.8 degC) in respect to CO_2 doubling has been quite invariant for almost 25 years (e.g. IPCC 2001). In this paper we concentrate our efforts on a major and well-identified deficiency of climate models, namely the representation of subtropical marine stratocumulus. This issue is considered of great magnitude as this leads to major deficiencies in the predicted global and regional climates (e.g. Jacob 1999; Klein and Hartmann 1993; Nigam 1997).

The purpose of this paper is, first, to advance the understanding of the physical processes that determine the thermal and dynamical state of the cloud-topped boundary layer and, second, to evaluate and improve methods of representing shallow-cloud systems in global climate models of the atmosphere. The evaluation of these methods and the respective improvement of the new parametrization schemes over current

* Corresponding author: Max-Planck-Institut für Meteorologie, Bundesstr. 55, 20146 Hamburg, Germany. e-mail: chlond@dkrz.de

schemes will be quantified by comparing single-column general-circulation model (GCM) diagnostics with similar diagnostics from detailed cloud-system realizations derived from a large-eddy simulation (LES) model in which the relevant coupled physical processes are as far as possible represented explicitly.

Previous studies on stratocumulus have focused mainly on the mean properties and concerned short time periods (Bechtold *et al.* 1996; Duynkerke *et al.* 1999). The full life cycle of stratocumulus needs now to be considered. The diurnal cycle problem is difficult and requires substantial computing resources to achieve the necessary resolution and length of integration. However, it is now timely to address the diurnal cycle of stratocumulus clouds with LES models, validated against comprehensive high-quality measurements.

As part of the EUROCS model intercomparison project, Duynkerke *et al.* (2004) compared properties and the evolution of stratocumulus as revealed by actual observations from the First International Satellite Cloud Climatology Project (ISCCP) Regional Experiment I (FIRE I) with some model simulations. The FIRE I experiment (Albrecht *et al.* 1988) provided a comprehensive observational set of data on marine stratocumulus on San Nicolas Island during July 1987. The goal of the model intercomparison was to study the diurnal variation of the turbulence and microphysical properties of a stratocumulus layer with specified initial and boundary conditions to assess the quality of the representation of stratocumulus clouds in GCMs.

This paper also addresses the full diurnal cycle of stratocumulus based on FIRE I observations. The methodology adopted rests upon the use of the single-column model (SCM) version of the European Centre Hamburg version (ECHAM) climate model (Roeckner *et al.* 1996, 2003) and the Max Planck Institute (MPI) LES model (Chlond 1992, 1994). The strategy applied here requires a two-stage procedure. In the first step the MPI–LES model is used to model explicitly the cloud-topped boundary layer and to produce comprehensive four-dimensional (4D) datasets of marine stratocumulus. Key processes and parametrization issues relevant for GCMs are addressed. These include diurnal variation of cloud properties, turbulence dynamics, and entrainment. In addition, ensemble simulations are performed in order to investigate the sensitivity of the model results to initial condition and external forcings. The second strategy step is to evaluate and improve the turbulence mixing scheme in the ECHAM–GCM. A powerful tool in this context is the use of the ECHAM–SCM representing a single column of the GCM with the same physical package as the full GCM. The intercomparison of the SCM results against the LES results enables the validation of the standard parametrization package and allows us to quantify the deficiencies in the various schemes. We evaluate the mixing scheme by turbulence only (and not the mixing by convection which is done by a mass-flux scheme). Reasons for deficiencies in the cloud-turbulence scheme were identified and physically grounded corrections are developed and implemented in the SCM and evaluated against the LES-generated datasets.

The paper is organized as follows. In section 2 a brief overview of the LES and the ECHAM–SCM model is given. The design of the numerical simulations is described in section 3. The LES results are presented and discussed in section 4. Section 5 provides results of the standard ECHAM–SCM. Based on our evaluation we applied a few modifications to the ECHAM–SCM, which include the vertical advection scheme, the numerical treatment of diffusion and radiation and the combination of the 1.5-order turbulent closure model with an explicit entrainment closure at the boundary-layer top. The implications of these modifications are shown for the presented EUROCS–FIRE case in section 5. Finally, summary and conclusions are given in section 6.

2. Model descriptions

(*a*) *The MPI–LES*

Over the past two decades, LES has become one of the leading methods to advance our understanding of processes in the planetary boundary layer, and particularly in the stratocumulus-topped boundary layer (e.g. Deardorff 1980; Moeng 1986; Moeng *et al.* 1992, 1995; Kogan *et al.* 1995; Khairoutdinov and Kogan 1999). The basic dynamical framework employed here is the MPI–LES model which has been described by Chlond (1992, 1994). The model includes most of the physical processes occurring in the moist boundary layer. It takes into account infrared radiative cooling in cloudy conditions (using a simple effective emissivity-like approach) and the influence of large-scale vertical motions. The subgrid-scale (SGS) model is based on a transport equation for the SGS turbulent energy (Deardorff 1980). To take into account the microphysical processes, Lüpkes' 3-variable parametrization scheme has been implemented (Lüpkes 1991). The runs use a computational domain of size $2.5 \times 2.5 \times 1.2\ \mathrm{km}^3$. The grid intervals are fixed to $\Delta x = \Delta y = 50$ m and $\Delta z = 10$ m. A time step of 2 s was used for all runs.

(*b*) *The ECHAM–SCM*

We use the SCM version of the ECHAM GCM. This atmospheric GCM used at the MPI is based on the weather forecast model of the European Centre for Medium Range Weather Forecasts (ECMWF). Numerous modifications have been applied to this model at the MPI and the German Climate Computing Centre (DKRZ) to make it suitable for climate forecasts, and it is now a model of the fifth generation. Previous versions of it have been successfully applied to a wide range of climate-related topics (e.g. Chen and Roeckner 1997; Lohmann and Feichter 1997; Manzini *et al.* 1997; Bacher *et al.* 1998; Moron *et al.* 1998). The main model physics are described in Roeckner *et al.* (1996, 2003). The physical parametrization package includes a bulk mass-flux convective parametrization scheme based on Tiedtke (1989) and Nordeng (1994). The turbulent surface fluxes are calculated from Monin–Obukhov similarity theory. Within and above the atmospheric boundary layer, a 1.5-order Turbulent Kinetic Energy (TKE) length-scale closure scheme is used to compute the turbulent transfer of momentum, heat, moisture and cloud water. This scheme has been described and evaluated in detail by Lenderink *et al.* (2000) and Lenderink and Holtslag (2000). In the standard model version, a 19-level hybrid sigma–pressure coordinate system is used. The vertical domain extends up to the pressure level of 10 hPa. For the SCM experiments conducted in this paper, we used the 40-level vertical grid, which gives a vertical resolution of about 100 m in the boundary layer, rather than the standard 19-level vertical grid because stratocumulus is only poorly resolved with the climate model's standard resolution.

3. Case description

In this paper we consider a simulation of the diurnal variation of stratocumulus. The simulation is defined in the EUROCS model-intercomparison project (Duynkerke *et al.* 2004), and is based on measurements during the FIRE I stratocumulus experiment performed off the coast of California in July 1987 (Albrecht *et al.* 1988). The case consists of a 37-hour simulation, starting at 0800 UTC (= 00 LT) on 14 July 1987 with idealized initial profiles and large-scale forcings. The initial and boundary conditions are based on observations described in Blascovic *et al.* (1991), Betts (1990), Hignett (1991)

and Duynkerke and Teixera (2001). The basic characteristics of the simulation are given here, but more specific and detailed information on the case is given in Duynkerke *et al.* (2004).

The initial conditions for the model were specified in the form of simplified vertical profiles of the liquid-water potential temperature, $\overline{\theta}_\mathrm{l}$ and the total water content, $\overline{q}$. The profiles were independent of height below the base of the inversion ($\overline{\theta}_\mathrm{l} = 287.5$ K, $\overline{q} = 9.6$ g kg^{-1}), and varied linearly with height between the base ($z = 595$ m) and the top ($z = 605$ m) of the inversion, and above the cloud, with jumps of $(\Delta\overline{q})_\mathrm{inv} = -3.0$ g kg^{-1} and $(\Delta\overline{\theta}_\mathrm{l})_\mathrm{inv} = 12$ K in the liquid-water potential temperature and the total water content across the inversion, respectively. The initial vertical gradients of $\overline{\theta}_\mathrm{l}$ and $\overline{q}$ within the free atmosphere were specified as 7.5×10^{-3} K m^{-1} and -3.3×10^{-3} g kg^{-1}m^{-1}, respectively. A uniform geostrophic wind was assumed $(u_\mathrm{g}, v_\mathrm{g}) = (3.4, -4.9)$ m s^{-1}, and the initial values for the velocity components u and v were also set to these values. An initial value for subgrid turbulent kinetic energy of 1 m^{2}s^{-2} was specified throughout the domain. The sea surface temperature and pressure were prescribed as $T_\mathrm{s} = 289$ K and $p_\mathrm{s} = 1012.5$ hPa, respectively. The specific humidity at the sea surface was set to its saturated value, namely 11.1 g kg^{-1}. The Coriolis parameter was set to $f = 8.0 \times 10^{-5}$ s^{-1} (corresponding to a latitude of about 33.3°N). The net long-wave radiation parametrization was a prescribed function of the liquid water path (LWP) and the net short-wave radiation was obtained from the analytical solution of the delta Eddington approximation (see Duynkerke *et al.* 2004 for details).

The large-scale (LS) divergence was set to 1×10^{-5} s^{-1}, resulting in a profile for the LS subsidence according to $w_\mathrm{LS} = -1.0 \times 10^{-5}\, z$ m s^{-1}, where z is in metres. In order to balance the subsidence heating and drying above the boundary layer, a LS advection term is included in the simulation:

$$\left(\frac{\mathrm{d}\theta_\mathrm{l}}{\mathrm{d}t}\right)_\mathrm{LS} = -7.5 \times 10^{-8} \cdot \max(z, 500)\ \mathrm{K\ s^{-1}} \qquad 0 \leqslant z \leqslant 1200\ \mathrm{m} \qquad (1)$$

$$\left(\frac{\mathrm{d}q}{\mathrm{d}t}\right)_\mathrm{LS} = 3.0 \times 10^{-11} \cdot \max(z, 500)\ \mathrm{kg\ kg^{-1}s^{-1}} \qquad 0 \leqslant z \leqslant 1200\ \mathrm{m}. \qquad (2)$$

All initial profiles were assumed to be horizontally homogeneous, except for the temperature field. In order to start the convective instability, spatially uncorrelated random perturbations, uniformly distributed between −0.1 K and 0.1 K, were applied to the initial temperature field at all grid points. In the reference run, drizzle formation due to coalescence was switched off (i.e. non-precipitating stratocumulus).

4. Results of LESs

(*a*) *Reference case*

(i) *Diurnal variation of the liquid water path.* The LES simulations were started at 0800 UTC (= 00 LT) on 14 July and lasted for 37 hours. We will concentrate on the diurnal variation of the stratocumulus deck as observed during FIRE I. We will use observations of 14 and 15 July 1987 and compare those with the model reference simulation. We will discuss the observed and simulated variations of LWP, and compare the modelled and observed turbulent quantities. To have an idea about the magnitude of statistical sampling error, ensemble runs of the reference case have been performed. The ensemble consists of 16 realizations of the process and uses the same numerical

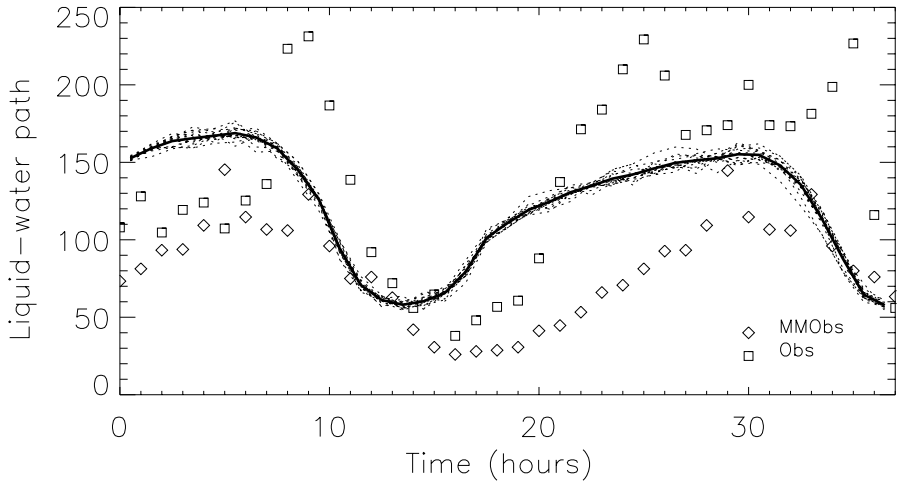

Figure 1. Time sequence of liquid-water path (g m^{-2}) of the stratocumulus case, observed by microwave radiometer (hourly mean, open squares) and generated from 16 large-eddy simulation model realizations (thin dashed lines), starting at 0800 UTC on 14 July 1987. The ensemble average is shown by the thick solid line, and the open diamonds represent the monthly mean diurnal variation.

set-up as described in section 3, but differs in that different sets of spatially uncorrelated random perturbations uniformly distributed between −0.1 and 0.1 K are used to initialize the temperature field. Figure 1 shows the variation of the simulated LWPs as a function of time, compared with the retrievals of a microwave radiometer from 14 and 15 July 1987. The LES model reproduces the strong diurnal variation in LWP due to the forcing imposed by the short-wave heating of the cloud layer. The ensemble of time series of the LWP is not widely scattered, indicating that the LWP which results from a volume integral of the liquid-water content can be determined with a high degree of statistical reliability. The maximum LWP is found around sunrise (which occurs at 05 LT), and the minimum of the LWP occurs shortly after local noon (12 LT). However, the thinning of the cloud layer is not sufficient to break up the cloud deck; in the simulations the cloud cover remains equal to one. Although the largest solar heating rates occur around solar noon, it is obvious that the diurnal changes in LWP do not follow the solar insolation directly, in the sense that they are symmetrical around local solar noon. This can be seen in both the observations and the simulation results. As a result of the large diurnal variation in LWP, the downward short-wave radiation does also not vary symmetrically around solar noon (not shown). In the LES the maximum solar insolation at the sea surface is reached at about 14 LT, two hours after local solar noon. It should be noted that the observed minimum in LWP appears to be about two hours after that in the LES, resulting in a much larger LWP in the simulation than in the observations during the afternoon. The cause for this difference cannot be specified and should be investigated further, as this might indicate too strong mixing in the LES, a deficiency in the radiation parametrization or a too simplified large-scale forcing.

(ii) *Turbulence structure.* In this section we will look at the simulated vertical turbulence structure of the stratocumulus-topped boundary layer and we will make some comparisons with the observations of Hignett (1991), who presented turbulence measurements collected by means of a tethered balloon during FIRE I. As in Duynkerke *et al.* (2004), we will concentrate on the total (resolved plus subgrid-scale) vertical

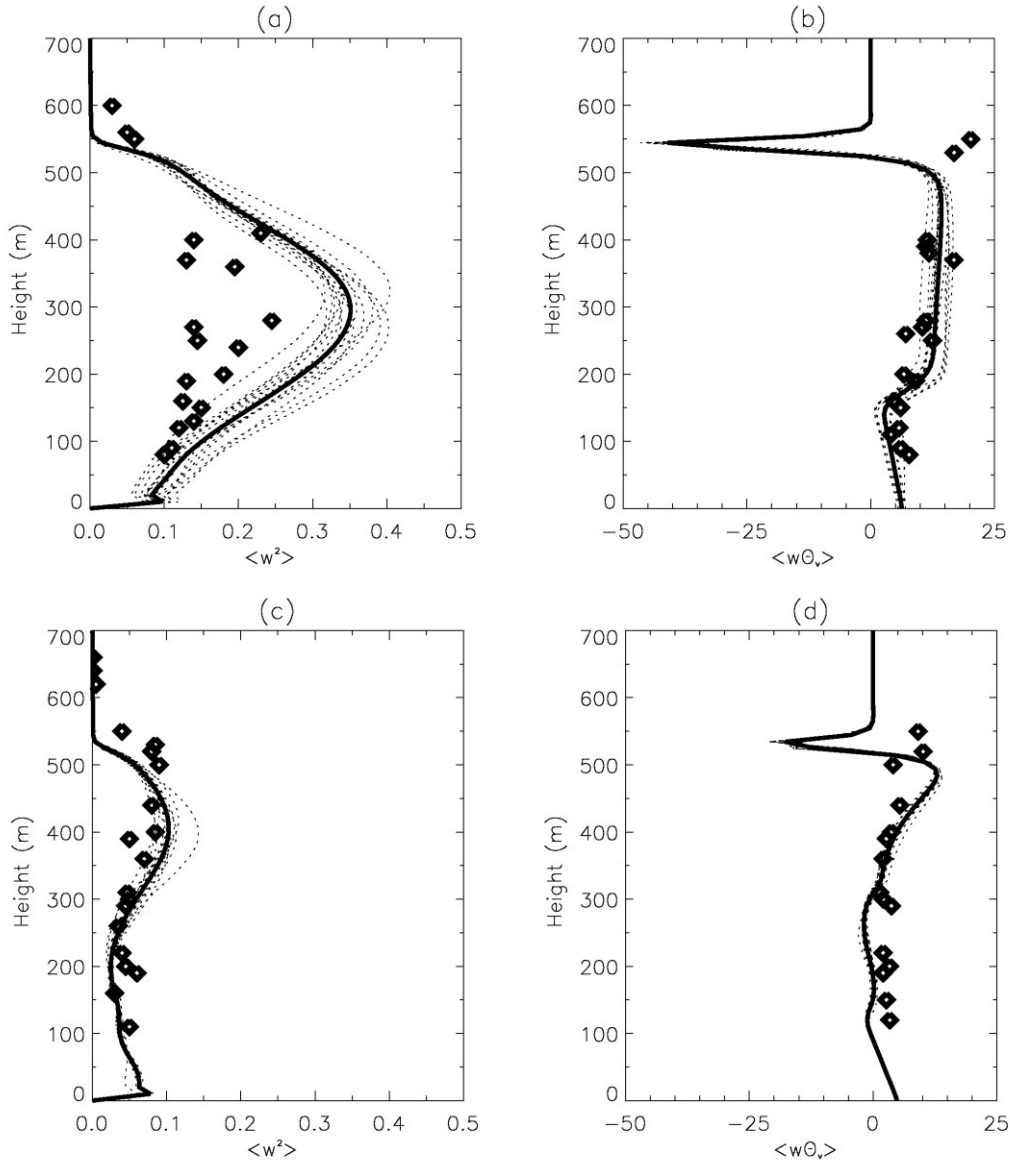

Figure 2. Vertical profiles of (a) total vertical velocity variances ($m^2 s^{-2}$) and (b) total buoyancy flux (W m^{-2}) during the night from tethered-balloon observations (diamonds) and generated from 16 large-eddy simulation model realizations (thin dashed lines) of the stratocumulus case. The modelled ensemble average is shown as a thick solid line. (c) and (d) are as (a) and (b) respectively, but for daytime. The calculated profiles are averages over one hour between 23 and 24 h (night) and between 36 and 37 h (day).

velocity variance $\overline{(w'^2)}$ which is an indicator of convective activity and the total buoyancy flux $\overline{(w' \cdot \theta'_v)}$, where θ_v denotes the virtual potential temperature. The periods chosen for comparison are centred around local noon and midnight, where LES results represent one-hour time averages. It can clearly be seen from Fig. 2 that results produced by LES agree reasonably well with the observations and are within the range of uncertainty in the observations, although the night-time vertical velocity variance seems to be slightly overpredicted by the LES model. The profiles generated

from the LES ensemble runs are not widely scattered, indicating that the one-hour time average is sufficient to produce reliable statistics for second-order moments. Obviously, there exist marked differences in the turbulence structure during daytime and night-time. During the night, both observations and calculations show that most of the buoyancy production is concentrated within the cloud layer. This implies that cloud-top coolings due to evaporation of cloud droplets and radiation are the dominant buoyancy production mechanisms. In this case the cloud-top cooling is strong enough to promote mixing all the way down to the sea surface. The nocturnal boundary layer is thus a well-mixed layer from the inversion to the surface, driven from cloud top in a manner analogous to that of a convective boundary layer heating from below. As a result, the maximum vertical velocity variance is located in the upper half of the boundary layer. During the daytime, the short-wave radiative heating becomes of the same magnitude as the long-wave radiative cooling for the cloud layer as a whole, but penetrates deeper into the cloud than the long-wave radiative cooling. As a result, the buoyancy flux at cloud base becomes slightly negative, tending to suppress vertical turbulent motions. This implies that the turbulent eddies driven from cloud-top cooling cannot now reach the surface. This situation is referred to as decoupling of the cloud layer from the subcloud layer and has been described in detail by Turton and Nicholls (1987) and Hignett (1991). To summarize, based on the intercomparison between observed and modelled turbulence statistics we conclude that the LES model is capable of reproducing the observed diurnal cycle of the boundary-layer structure reasonably well.

(*b*) *Sensitivity runs*

(i) *Impact of drizzle.* The fundamental approach of LES is to explicitly resolve large turbulent eddies, which contain most TKE and do most transport. Although LES explicitly resolves the most important eddies, uncertainties still exist in these simulations. There is always uncertainty due to numerics and due to the treatment of small-scale turbulent motions through a SGS model. Moreover, in a cloud-topped boundary layer other uncertainties arise from the fact that the effects of condensation/evaporation and precipitation are parametrized processes in LESs.

To examine the sensitivity of our LES results arising from the formation of drizzle, we have performed one additional run. The reference run is labelled REFERENCE and refers to a non-precipitating stratocumulus simulation. The run DRIZZLE refers to the run which uses Lüpkes' (1991) microphysical scheme. Both runs utilize the same model initialization and forcing (see section 3).

Figure 3 displays the time evolution of (a) the inversion height, (b) LWP, and (c) the precipitation rate for both runs. Both versions of the model produce a solid cloud cover and show a distinct diurnal cycle. However, the REFERENCE run produces a deeper boundary layer and a larger LWP than the DRIZZLE run. Note that the time variation of the boundary-layer top is directly proportional to the entrainment rate as it is given by the difference between the entrainment velocity and the large-scale subsidence. Therefore, these results suggest that the primary dynamical effect of drizzle is to reduce the buoyant production of TKE. Less production of TKE results in a shallower boundary layer due to a reduction in entrainment rates. Drizzle also acts to limit the LWP of stratocumulus. We found that the removal of water by drizzle lowered the maximum liquid-water content near cloud top by about 20%. These key results have also been reported by Stevens *et al.* (1998) and Chlond and Wolkau (2000). Finally, the precipitation rate at the surface in the DRIZZLE run is rather small, attaining values varying between 0 and 0.4 mm d^{-1}. The simulated precipitation rates were too small to significantly alter

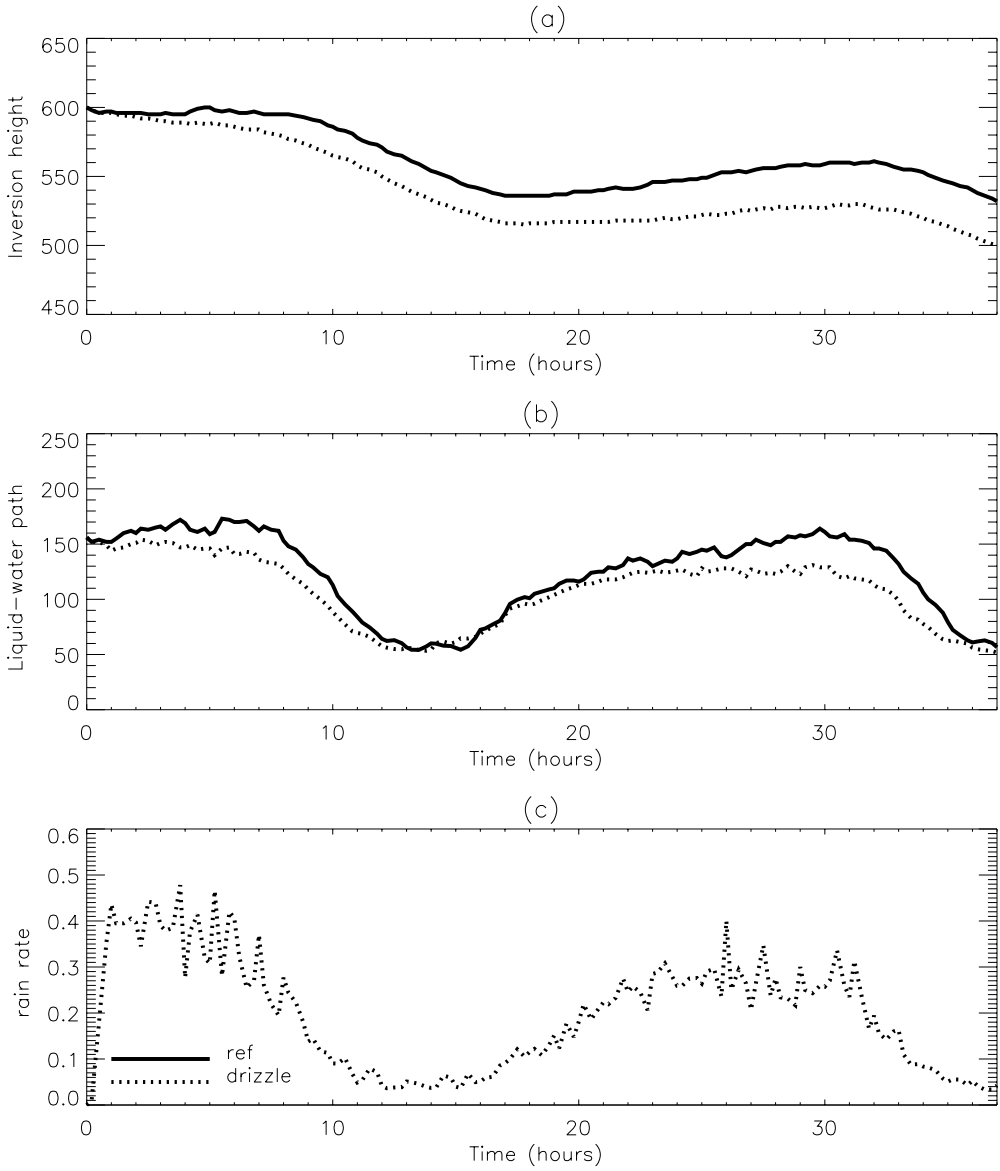

Figure 3. Time evolution of (a) inversion height (m), (b) liquid-water path (g m^{-2}), and (c) precipitation rate (mm d^{-1}) for two large-eddy simulation runs: 'ref' (solid) is the non-precipitating stratocumulus simulation, and 'drizzle' (dotted) is the run using the Lüpkes (1991) microphysical scheme.

the vertical distribution of latent heating to produce a different boundary-layer regime. In addition, it is striking that the daytime minimum LWPs are nearly the same for the REFERENCE and the DRIZZLE simulation, which indicates that the continuous loss of liquid water due to drizzle does not lead to a systematic lower LWP. This seems to suggest that negative feedbacks are present in the system counteracting the liquid water loss due to drizzle. The stabilizing effects in the DRIZZLE simulation are due to a reduced entrainment rate of dry warm air from above the inversion and due to an increase of the surface latent heat flux as a result of larger jumps in specific humidity

between the sea surface and the sub-cloud layer. Both effects may compensate for the loss of moisture due to drizzle.

(ii) *Sensitivity of LES results to environmental conditions.* In this section we address the parametric uncertainty of our LES results that arises because of the incomplete knowledge of model input parameters. The importance of these parameters to model outputs can be ranked by using a sensitivity analysis. In a sensitivity analysis we are interested in how the model outputs respond to small changes in a given uncertain parameter with all of the other parameters fixed. In this way the sensitivity analysis reveals the local gradient of the model response with respect to a given parameter. Here, we examine the sensitivity of our LES results with respect to the assumed values of various external environmental conditions. These conditions include all those environmental parameters that are needed to specify all the mean initial and boundary conditions required to run a model simulation. Our study investigates the sensitivity of the model output with respect to: (1) the inversion strength in total water content $(\Delta\overline{q})_{\rm inv}$, (2) the inversion strength in liquid-water potential temperature $(\Delta\overline{\theta}_{\rm l})_{\rm inv}$, (3) the large-scale subsidence $w_{\rm LS}$, (4) the sea surface temperature, and (5) the net long-wave radiative cooling from the cloud top, $F_{\rm NET}^{\rm CT}$. Uncertainties in these external input parameters may arise from instrumental measurement errors, sampling errors, and the non-stationarity and spatial inhomogeneities of the fields under consideration during the measurements.

To derive a quantitative measure of the uncertainty of modelled target variables, we adopt a methodology for objective determination of the uncertainty in LES-derived quantities. The methodology is based on standard error-propagation procedures and yields expressions for probable error as a function of the relevant parameters (Chlond and Wolkau 2000).

For any LES-derived function Ψ (i.e. $\langle q_{\rm l}\rangle$, $\langle w\theta_{\rm v}\rangle$, $\langle wq_{\rm t}\rangle$, $\langle w^2\rangle$, etc., where $\langle\ \rangle$ denotes the horizonal averaging operator) that depends on several measured environmental parameters a, b, etc. (i.e. $(\Delta\overline{q})_{\rm inv}$, $(\Delta\overline{\theta}_{\rm l})_{\rm inv}$, $w_{\rm LS}$, T_0, $F_{\rm NET}^{\rm CT}$), the uncertainty σ_Ψ (standard deviation) in Ψ can be approximated as:

$$\sigma_\Psi^2 = \left(\frac{\partial\Psi}{\partial a}\right)^2\sigma_a^2 + \left(\frac{\partial\Psi}{\partial b}\right)^2\sigma_b^2 + 2C_{ab}\left(\frac{\partial\Psi}{\partial a}\right)\left(\frac{\partial\Psi}{\partial b}\right) + \cdots\ , \tag{3}$$

where σ_a is the uncertainty in the measured parameter a and C_{ab} is the covariance between the measured parameters a and b. Assuming uncorrelated measurement errors we obtain

$$\sigma_\Psi = \sqrt{\sum_i \left(\frac{\partial\Psi}{\partial x_i}\right)^2\sigma_{x_i}^2}, \tag{4}$$

where x_i $(i = 1, 5)$ denote the external environmental parameters, that is, $x_1 = (\Delta\overline{q})_{\rm inv}$, $x_2 = (\Delta\overline{\theta}_{\rm l})_{\rm inv}$, $x_3 = w_{\rm LS}$, $x_4 = T_0$, and $x_5 = F_{\rm NET}^{\rm CT}$, Thus, the total uncertainty (standard deviation) of a LES-derived quantity Ψ contains contributions from uncertainties due to thermodynamic measurements of cloud-top jumps of liquid-water potential temperature and total water content, errors in the estimation of the large-scale subsidence and sea surface temperature, and errors in the assumed value of the net radiative cooling. To evaluate the above equation, we must first evaluate the partial derivative of Ψ with respect to the parameters x_i. This has been done by performing 10 LES runs in which one of the parameters x_i has been varied (positively and negatively around its central value)

TABLE 1. DETAILS OF EXTERNAL ENVIRONMENTAL INPUT PARAMETERS

Parameter	Units	Central value	Standard deviation
Total water content change at inversion, $(\Delta\overline{q})_{\rm inv}$	g kg^{-1}	−3.0	0.5
Liquid-water potential temperature change at inversion, $(\Delta\overline{\theta}_{\rm l})_{\rm inv}$	K	12.0	1.0
Large-scale subsidence, $w_{\rm LS}$	m s^{-1}	−0.012	0.0018
Sea surface temperature, T_0	K	289.0	0.5
Net long-wave radiating cooling at cloud top, $F_{\rm NET}^{\rm CT}$	W m^{-2}	70.0	10.5

TABLE 2. RESULTS OF LARGE-EDDY SIMULATION SENSITIVITY ANALYSIS

Parameter		Units	Mean	Standard deviation	Normalized variance contributions (%) by various parameters, x_i				
					x_1/s_1	x_2/s_2	x_3/s_3	x_4/s_4	x_5/s_5
Buoyancy flux, $\langle w\theta_{\rm v}\rangle_{\max}$	(night)	W m^{-2}	12.6	2.9	34.8/+	14.8/−	21.4/+	0	29.0/+
	(day)	W m^{-2}	11.1	2.7	<1	<1	<1	0	98.7/+
Vertical velocity	(night)	m^{2}s^2	0.36	0.080	0	0	0	0	100.0/+
variance, $\langle w^2\rangle_{\max}$	(day)	m^{2}s^2	0.14	0.025	0	0	0	0	100.0/+
Liquid-water path, LWP	max	g s^{-2}	152	42.5	54.9/−	1.3/+	25.6/−	0	18.2/+
	min	g s^{-2}	56	13.5	56.9/−	5.6/+	11.1/−	0	26.4/+
Entrainment rate, $w_{\rm e}$		cm s^{-1}	0.52	0.093	<1	26.8/−	6.6/+	0	65.9/+

$x_1 = (\Delta\overline{q})_{\rm inv}$, $x_2 = (\Delta\overline{\theta}_{\rm l})_{\rm inv}$, $x_3 = T_0$, $x_4 = w_{\rm LS}$, $x_5 = F_{\rm NET}^{\rm CT}$ (see text for details).

while the others have been kept fixed to their original values. The partial derivative is then calculated using a second-order accurate finite-difference approximation.

With respect to the jumps of liquid-water potential temperature and total water content, we assume that these values are accurate within the range ± 1 K and ± 0.5 g kg^{-1}, respectively. The sea surface temperature was assumed to be accurate within the range ± 0.5 K. With regard to the large-scale subsidence and the net long-wave radiative cooling, we anticipate that these quantities can be estimated from the measurements with an accuracy of 15%. Admittedly, an accuracy of 15% for measurements of large-scale subsidence is very optimistic (cf. Stevens *et al.* (2003), who gave errors bars of 50% from their observed estimate of subsidence from the second Dynamics and Chemistry of Marine Stratocumulus field study, for example). However, we used this conservative estimate in order to apply the sensitivity analysis which relies on linear relationships between the variances of the simulated quantities and the variances of measured environmental parameters. Central values and uncertainty factors (standard deviations) of the external environmental input parameters are listed in Table 1.

The sensitivity analysis provides a framework for ranking the uncertain parameters according to their contribution to the total model variance. Table 2 gives means and standard deviations of the maximum total (resolved plus subgrid-scale) buoyancy flux and the maximum total vertical velocity variance occurring in the domain (that is, $\langle w\theta_{\rm v}\rangle_{\max}$ and $\langle w^2\rangle_{\max}$) as well as of the entrainment rate $w_{\rm e}$, and the maximum and the minimum LWP. In addition, normalized variance contributions (in percent) from variations of external input parameters x_i (that is, $(\Delta\overline{q})_{\rm inv}$, $(\Delta\overline{\theta})_{\rm inv}$, T_0, $w_{\rm LS}$, $F_{\rm NET}^{\rm CT}$)

to the total variance σ_Ψ^2 of a modelled quantity Ψ and the sign of the derivatives $s_i = \partial\Psi/\partial x_i$ are also listed.

In particular, the maximum buoyancy flux which is found in the upper part of the cloud layer (see Fig. 2) takes a mean value of 12.6 (11.1) W m^{-2} during the night (day). This implies that cloud-top cooling due to evaporation of cloud droplets and radiation are the dominant buoyancy production mechanisms. The model predicts an uncertainty interval ($\pm\sigma$ interval) for the buoyancy flux of 9.7–15.5 (8.4–13.8) W m^{-2} at 2330 LT (1230 LT) where the parameters $(\Delta\overline{q})_{\rm inv}$ and $F_{\rm NET}^{\rm CT}$ make the largest contribution to the model variance (see Table 2). The modelled magnitude of the vertical velocity variance is in a fair agreement with the observations (see Fig. 2). The net long-wave radiative flux divergence $F_{\rm NET}^{\rm CT}$ is exclusively responsible for the modelled uncertainty (see Table 2), indicating that the convection is driven due to cooling from cloud top. However, it is striking that the parameters x_1, x_2 and x_3 have impact on the maximum buoyancy flux, but not at all on the vertical velocity variance. This is surprising since the buoyancy flux is the major production term of vertical velocity variance. To resolve this discrepancy we have inspected the buoyancy profiles which show that, in contrast to the maximum value, the integral of the buoyancy flux over the cloud layer is almost unaffected by variations of these parameters. The uncertainty range for the modelled LWP is rather large ($\pm$42.5 g kg^{-1} at 2330 LT and $\pm$13.5 g kg^{-1} at 1230 LT). The inversion jump in total water $(\Delta\overline{q})_{\rm inv}$ makes the largest contribution to the model variance, where larger jumps in $(\Delta\overline{q})_{\rm inv}$ produce smaller peak values in LWP and vice versa (see Table 2). It might appear amazing that the LWP is not sensitive to the large-scale subsidence rate, since pushing down the cloud top harder (softer) should give a shallower (deeper) cloud, all other things being equal. However, one should realize that in these runs in accord with the subsidence rate also the large-scale advective forcing (see Eqs. (1) and (2)) has been adjusted in order to balance the subsidence heating and drying above the inversion, respectively. As a consequence, a larger (smaller) subsidence rate results also in more (less) cooling and moistening of the boundary layer, respectively. This in turn has an indirect influence on the evolution of the cloud base producing a lower (higher) cloud base in case of a larger (smaller) subsidence rate. Therefore, based on these facts, the insensitivity of the LWP with respect to $w_{\rm LS}$ appears reasonable. Finally, we note that the mean value of the modelled entrainment rate $w_{\rm e}$ is 0.52 cm s^{-1} with an uncertainty range of 0.093 cm s^{-1}. The parameters $F_{\rm NET}^{\rm CT}$, and the cloud top jump in liquid-water potential temperature $(\Delta\overline{\theta}_{\rm l})_{\rm inv}$ make the largest contributions to the modelled uncertainty (see Table 2).

5. SCM RESULTS

(*a*) *Standard model*

We first show results for a SCM with the standard ECHAM5 configuration. We ran the model with a vertical resolution of 40 levels, of which 12 are in the lowest kilometre of the atmosphere. The time step is 900 s.

Figure 4 shows observed and modelled LWP from the SCM as function of time. The SCM predicts a solid cloud cover and reproduces a fair representation of the diurnal cycle as the LWP varies between 100 g m^{-2} around sunrise to about 20 g m^{-2} some hours before sunset. However, compared to the observations, the SCM predicts a too low LWP and thus tends to thin the stratocumulus layer too quickly. Subsequently, in the SCM this leads to a much larger amount of downwelling short-wave radiation absorbed at the sea surface causing an erroneous warming bias of the sea surface temperature. Typically, the liquid-water content varies linearly with height. As a result the LWP is

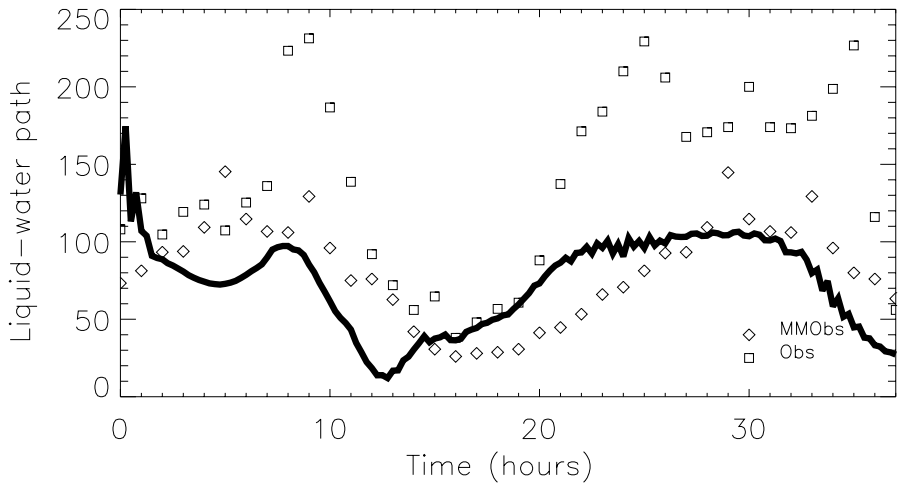

Figure 4. Time sequence of observed (open squares) and simulated (solid line) liquid-water path (g m^{-2}) using the standard single-column model for 14 and 15 July 1987. Diamonds show the monthly mean diurnal variation.

proportional to the cloud thickness squared (Blascovic *et al.* 1991). Realizing the large sensitivity of the LWP with cloud thickness, this implies that even small errors due to the coarse vertical resolution of current operational GCMs or due to an incorrect description of the entrainment fluxes at cloud top can give rise to large errors in the modelled LWP and subsequently to large errors in the surface energy balance.

Another serious error of the standard SCM becomes apparent by inspection of the TKE. Figure 5 displays the evolution of the TKE in a time–height slice. The TKE simulated with the SCM shows very little resemblance to the results of the LES model and to the observations. The model produces erroneously large levels of TKE up to 12 $m^2 s^{-2}$. One may argue that TKE is not an important prognostic variable in a SCM/GCM. However, since TKE is closely related to the diffusion coefficients and hence tied to the fluxes of dynamic and thermodynamic quantities, it is a sensitive indicator of the quality of the vertical fluxes. Moreover, aerosol/microphysical parametrization schemes in GCMs utilize the square root of the TKE as a measure for a typical vertical updraft velocity to calculate supersaturations within clouds (e.g. Ghan *et al.* 1997). Therefore, TKE is an important quantity and should be represented reasonably well.

The phenomenon of too large TKE levels was already discovered and described by Lenderink and Holtslag (2000) who showed that the numerical solution corresponds to a too unstable stratified upper-cloud layer in which too much TKE is produced by buoyancy forces.

To circumvent the time-step dependency of the numerical solution of the radiation–diffusion equation, we adopt a strategy that was proposed by the ECMWF (White 2000). Basically, the solution is based on the application of the 'fractional steps' method (Beljaars 1991). This procedure requires that the radiative tendency is first computed explicitly. Then this radiative tendency is passed to the diffusion routine, and the diffusion routine subsequently solves the whole system implicitly, including the radiative tendency on the right-hand side of the diffusion equation. Due to this coupling of diffusive and radiative processes, a time-step-independent equilibrium solution can be enforced.

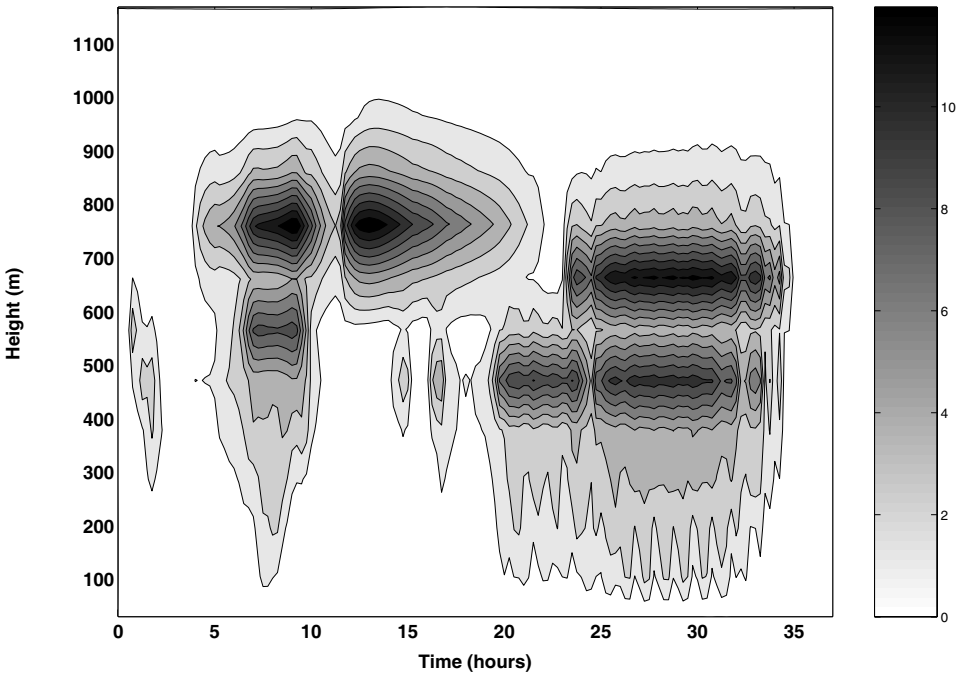

Figure 5. Time-height section of turbulent kinetic energy (m^2s^{-2}) in the stratocumulus simulation using the standard ECHAM5 single-column model.

(*b*) *Revised model*

Based on the findings described above, we modified the numerics of the SCM and also made a few modifications to the standard turbulence scheme. In this section we will show that the behaviour of the model for this case can be significantly improved by applying certain modifications.

First, we modified the time integration scheme in a manner described in the previous subsection. The new scheme removes the time-step dependency of the numerical solution of the old process-splitting scheme and reproduces the correct radiative-diffusive equilibrium.

Second, we replaced the centred-difference scheme which was used to model the vertical large-scale advection by an upstream scheme. This removes an instability which is intimately connected to the occurrence of so-called 'wiggles' (i.e. unphysical oscillations) generated by the numerical advection of steep gradients of a transported thermodynamic quantity (i.e. the numerical scheme produces over- and undershoots).

Third, we modified the formulation of the turbulent length-scale. Realistic simulation of planetary boundary layers requires a suitable specification of the master length-scale. In the standard SCM the length-scale λ is specified according to

$$\lambda = S(Ri)l(z). \tag{5}$$

Here $l(z)$ is the Blackadar (1962) length-scale ($1/l(z) = 1/(\kappa z) + 1/\Lambda$, with von Kármán constant $\kappa = 0.4$ and the asymptotic length-scale $\Lambda = 300$ m), and $S(Ri)$ is a stability correction function which depends on the moist Richardson number Ri. In ECHAM5 the stability corrections are of the usual 'Louis type' (Roeckner *et al.* 1996; Lenderink *et al.* 2000). We replaced this length-scale formulation by another one which was proposed by Bougeault and Lacarrère (1989). It is based on a physically founded

concept and the length-scale of the largest turbulent eddies at a given level is determined as a function of the buoyancy profile of adjacent levels. The algorithm relies on the computation of the maximum vertical displacement allowed for a parcel of moist air having the mean kinetic energy of the departure level as initial kinetic energy. This method allows the length-scale at any level not only to be affected by the stability at this level, but also to be influenced by the effect of remote stable zones ('non-local' length-scale). Since this parcel length-scale reflects the internal stratification of the boundary layer, it seems theoretically more appropriate.

The fourth modification concerned the implementation of an explicit entrainment parametrization to specify the vertical fluxes of heat and moisture at the boundary-layer top. This approach permits a realistic treatment of a stratocumulus-topped boundary layer even in a SCM/GCM with coarse vertical resolution and combines the ordinary 1.5-order turbulent closure model with an explicit entrainment formulation. To represent the entrainment interface on a discrete vertical grid, we applied a numerical front tracking/capturing method which allows the computation of propagating phase boundaries in fluids (Zhong *et al.* 1996). This approach is similar in spirit to the 'prognostic inversion' approach described in Grenier and Bretherton (2001, in the following denoted as GB) who should be credited for this inversion treatment. Both methods share the property that the inversion height is prognostically computed and that they combine an internally varying boundary-layer depth with an entrainment parametrization. The advantage of this formulation is that it permits the stratocumulus top to lie between grid levels and to evolve continuously with time. This is a desirable feature for the simulation of stratocumulus clouds because cloud feedbacks on turbulence and radiation can be captured despite the coarseness of the grid. Perhaps the GB and the front tracking/capturing algorithm have even more in common. However, in contrast to the front tracking/capturing algorithm presented here, subtle details of the 'prognostic inversion' approach have not been described in the GB paper. Moreover, the approach described here appears more general as it allows, with some modification, treatment of the nucleation and interaction of phase boundaries (see Zhong *et al.* 1996). As already mentioned in GB, a disadvantage of the prognostic approach is that it appears impractical to implement in a 3D host numerical model in which all other processes such as horizontal advection are computed on a fixed grid. For this reason GB and also Lock (2001) proposed a method which is based on a 'profile reconstruction' technique to diagnose the height of the discontinuous inversion. They demonstrated that this solution of the problem has the advantage of a much improved representation of stratocumulus-capped boundary layers, not only in SCMs but also in a climate-resolution GCM. At the end of section 6 we will show how the front tracking/capturing method proposed here can be extended in order to be suitable for 3D applications.

The stratocumulus-topped boundary layer is usually topped by a stratified entrainment interface, in which large turbulent motions drive smaller entraining eddies that incorporate free-tropospheric air into the boundary layer. To parametrize this process we use here a very simple parametrization for the entrainment rate, w_e, which was derived in the limits of no surface fluxes and a vanishingly thin inversion layer (e.g. Stull 1988), namely

$$w_e = C \cdot \frac{\Delta F_{tot}/(\rho \cdot c_p)}{\Delta \theta_v}, \tag{6}$$

where ΔF_{tot} is the total (long-wave and short-wave) radiative cooling in the cloud layer, ρ and c_p are the density and the specific heat at constant pressure, respectively, for air, $\Delta \theta_v$ is the virtual potential temperature jump across the inversion, which is a measure

of the buoyancy jump here. Therefore, large changes in the radiative cooling at cloud top promote entrainment, whereas large buoyancy jumps at cloud top tend to inhibit entrainment. In Eq. (6), C is a nondimensional parameter which should depend on the mixing efficiency, the fraction of the radiative flux divergence across the inversion layer and should also account for evaporative cooling feedback on entrainment. Here we treat C as an empirical constant of the current entrainment model, and we take $C = 1$ for simplicity. Whether this entrainment parametrization is appropriate is a matter of debate (e.g. Lock 1998; Lock and MacVean 1999; Moeng *et al.* 1999; Stevens 2002; van Zanten *et al.* 1999). However, we use this simple parametrization as a proxy of a typical entrainment parametrization; of course, any other entrainment scheme could be implemented in the SCM instead. To check the skill of the entrainment parametrization, we evaluate Eq. (6) using representative values of the radiative cooling and the virtual potential temperature jump across the inversion from the FIRE case discussed here. For the nocturnal boundary layer, with $\Delta F_{\mathrm{tot}}/(\rho \cdot c_p) = 0.06$ K m s^{-1} and $\Delta\theta_{\mathrm{v}} = 10$ K, Eq. (6) gives a value of $w_{\mathrm{e}} = 0.0060$ m s^{-1} which gives a reasonable entrainment rate compared to that seen in the LES where we derive a value of $w_{\mathrm{e}} = 0.0055$ m s^{-1}. In accordance with LES, Eq. (6) gives smaller values for the entrainment rate during the day as ΔF_{tot} is reduced due to the short-wave heating.

To illustrate the front tracking/capturing method we consider the following equation

$$\frac{\partial}{\partial t}\overline{\psi} + \frac{\partial}{\partial z}(\overline{w} \cdot \overline{\psi}) = -\frac{\partial F}{\partial z} + s, \tag{7}$$

where $\overline{\psi}$ denotes any thermodynamic variable, $\overline{w}$ is the large-scale vertical velocity, s is a source term, and F is the turbulent flux of ψ, i.e.

$$F = \overline{w' \cdot \psi'}. \tag{8}$$

The turbulent fluxes of ψ within the PBL are computed using an eddy diffusivity K (which is related to the TKE according to the assumptions made in the 1.5-order closure):

$$\overline{w' \cdot \psi'} = -K \cdot \frac{\partial}{\partial z}\overline{\psi}. \tag{9}$$

At the entrainment interface at height z_i, the turbulent flux of ψ is parametrized according to the formulation of Lilly (1968), namely

$$\overline{w' \cdot \psi'} = -w_{\mathrm{e}} \cdot \Delta\psi, \tag{10}$$

where $\Delta\psi$ is the jump in $\overline{\psi}$ across the inversion layer which is assumed to be infinitely thin.

We use the following notation. As variables meshes will be used, we denote by $x^n_{k+1/2}$ the position of the right cell boundary of the grid cell with the index k. Subsequently $(x^n_{k-1/2}, x^n_{k+1/2})$ represents a computational cell, x^n_k is the centre of the cell, and $h^n_k = x^n_{k+1/2} - x^n_{k-1/2}$ is the cell width at time t_n. (For simplicity we assume that we have initially a homogeneous mesh with a grid interval h.) Since we do not want to shift all grid points, the algorithm only shifts grid points locally. As a result, we will have only a locally nonuniform mesh due to two cells moving with the entrainment interface in a certain way. Assume that at time t_n, $x^n_{k_0+1/2}$ represents the position of the entrainment interface. At time t_{n+1}, $x^{n+1}_{k_0+1/2}$ moves to a new position. Instead of letting all grid points move with the entrainment interface, we move only the cell boundary with the index $k_0 + 1/2$. As a consequence, subsequently the locations of the cell centres with

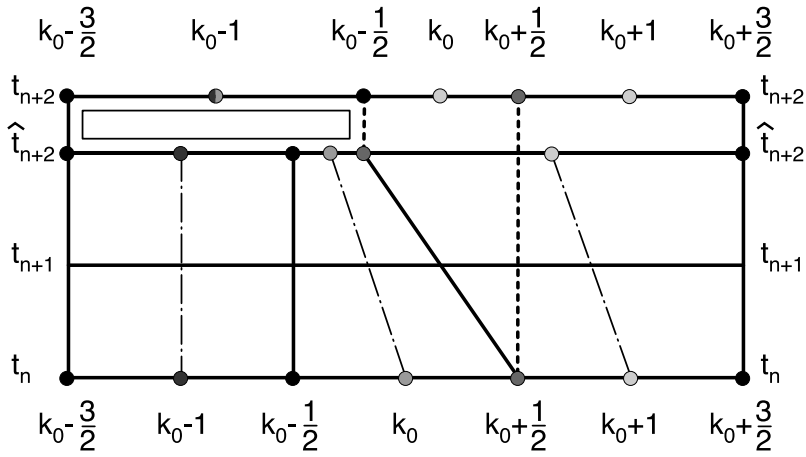

Figure 6. A computational mesh in the (z, t) plane, showing the local shifting of grid points. To illustrate the re-indexing process, the grid set-up is shown at t_n, t_{n+1}, $\widehat{t}_{n+2}$ and t_{n+2}. The intermediate state $\widehat{t}_{n+2}$ characterizes the situation that violates the non-re-indexing condition (see text). The state at t_{n+2} displays the grid set-up after the regridding step has been performed (after Zhong *et al.* 1996).

the indices k_0 and $k_0 + 1$ are changed (see Fig. 6). By doing this, the size of cells k_0 and $k_0 + 1$ will change as time proceeds: one cell will shrink, the other will be enlarged. When one cell gets too small, the location of one grid point is adjusted. If $\overline{\psi}(t, z)$ is given, the cell average of $\overline{\psi}$ in cell k and at time t_n is defined as

$$\psi_k^n = \frac{1}{h_k^n} \cdot \int_{x_{k-1/2}^n}^{x_{k+1/2}^n} \psi(t_n, z) \cdot \mathrm{d}z. \tag{11}$$

Given the approximate solution $\{\psi_k^n\}$ at time t_n, the algorithm then works as follows. (For simplicity, we have used here the forward Euler time differencing scheme to write down the discrete equations. Of course, the method can easily be adapted to other time-differencing schemes.)

1. Compute ψ_k^{n+1} from the discrete version of Eq. (7) for all cells not containing the entrainment interface (i.e. $\{\psi_k^{n+1}, \forall k \wedge (k \neq k_0) \wedge (k \neq k_0 + 1)\}$) according to

$$\begin{aligned}\psi_k^{n+1} = \psi_k^n &- \{(\overline{w} \cdot \psi)|_{k+1/2}^n - (\overline{w} \cdot \psi)|_{k-1/2}^n\} \cdot \Delta t / h_k^n \\ &- (F_{k+1/2}^n - F_{k-1/2}^n) \cdot \Delta t / h_k^n + s_k^n \cdot \Delta t.\end{aligned} \tag{12}$$

2. Compute the entrainment interface propagation speed, w_{ps}, according to the relation

$$w_{\mathrm{ps}} = \overline{w} + w_{\mathrm{e}}. \tag{13}$$

3. Shift grid point locally by distinguishing two cases:

(a) If $w_{\mathrm{ps}} < 0$:

• Shift the entrainment interface at $k_0{+}1/2$ according to $x_{k_0+1/2}^{n+1}{=}x_{k_0+1/2}^n{+}w_{\mathrm{ps}} \cdot \Delta t$ and compute the cell averages in the cells k_0 and $k_0 + 1$ from the formulae:

$$\begin{aligned}\psi_{k_0}^{n+1} = \psi_{k_0}^n \cdot h_{k_0}^n / h_{k_0}^{n+1} &+ \{(\overline{w} \cdot \psi)|_{k_0-1/2}^n + w_{\mathrm{e}} \cdot \psi_{k_0+1}^n\} \cdot \Delta t / h_{k_0}^{n+1} \\ &+ F_{k_0-1/2}^n \cdot \Delta t / h_{k_0}^{n+1} + s_k^n \cdot \Delta t \cdot h_{k_0}^n / h_{k_0}^{n+1}\end{aligned} \tag{14}$$

and

$$\psi_{k_0+1}^{n+1} = \psi_{k_0+1}^{n} \cdot h_{k_0+1}^{n} / h_{k_0+1}^{n+1} - \{(\overline{w} \cdot \psi)|_{k_0+3/2}^{n} + w_e \cdot \psi_{k_0+1}^{n}\} \cdot \Delta t / h_{k_0+1}^{n+1} - F_{k_0+3/2}^{n} \cdot \Delta t / h_{k_0+1}^{n+1} + s_{k_0+1}^{n} \cdot \Delta t \cdot h_{k_0+1}^{n} / h_{k_0+1}^{n+1}. \quad (15)$$

• If $|x_{k_0-1/2}^{n+1} - x_{k_0+1/2}^{n+1}| > h/2$ do nothing, otherwise adjust the location of the point $k_0 - 1/2$ in the following way: Move the point $k_0 - 1/2$ to the right side of the entrainment interface and relabel it as $k_0 + 1/2$, so that the cell $(x_{k_0+1/2}^{n+1}, x_{k_0+3/2}^{n+1})$ keeps a regular size of $O(h)$. Relabel the entrainment interface as $k_0 - 1/2$. Change positions of $k_0 - 1$, k_0, $k_0 + 1$ accordingly for the three adjusted cells (see Fig. 6). Then recompute the cell averages associated with the modified cells (regridding step). The regridded ψ_{k_0-1} is simply the weighted average of the old ψ_{k_0-1} and ψ_{k_0}, where old and new refer to before and after regridding. For the indices k_0 and $k_0 + 1$ the regridded values are: $(\psi_{k_0})_{\text{new}} = (\psi_{k_0+1})_{\text{old}}$ and $(\psi_{k_0+1})_{\text{new}} = (\psi_{k_0+1})_{\text{old}}$.

(b) If $w_{ps} \geqslant 0$, the procedure is similar to that of the case $w_{ps} < 0$:

• Shift the entrainment interface at $k_0+1/2$ according to $x_{k_0+1/2}^{n+1} = x_{k_0+1/2}^{n} + w_{ps} \cdot \Delta t$ and compute the cell averages in the cells k_0 and $k_0 + 1$. Formulae are similar to Eqs. (14) and (15).

• If $|x_{k_0+1/2}^{n+1} - x_{k_0+3/2}^{n+1}| > h/2$ do nothing, otherwise modify the location of the grid point $k_0 + 3/2$ and compute the cell averages for the adjusted cells.

4. Repeat steps 1–3.

Finally it should be noted that, for this Lagrangian interface tracking algorithm, the restriction $|w_{ps} \cdot \Delta t / h| < 1/2$ is necessary for its stability. This is due to the fact that the computational cell can shrink as time proceeds and that a shrunken cell must be large enough compared to h in order to avoid instability.

Before presenting results of the revised scheme, we would like to comment on the relative importance of the applied changes. Steps 1 and 2 are concerned with the numerical stability of the scheme and remove high-frequency numerical noise. However, these measures cannot prevent the scheme from being too diffusive, as the combination of the turbulence scheme with the numerical representation of subsidence produces unphysical 'numerical entrainment'. This type of error was already identified by Lenderink and Holtslag (2000) who found that entrainment appears to be related to the representation of the cloud in an Eulerian grid and not to the physics of the turbulence scheme. At coarse resolution (vertical grid spacing of the order of 100 m as commonly used in operational models), this process dominates the solution producing an erroneous strong dependence of the entrainment rate on the subsidence rate. As a result, the inversion top either gets 'locked in' to a fixed grid level or the boundary-layer height is not correctly predicted. Therefore, the most important step with respect to the improvement of the scheme is related to the implementation of the front tracking/capturing method in conjunction with the explicit entrainment parametrization. This measure allows a much improved representation of the stratocumulus-topped boundary layer as this method treats advection, radiation and the turbulent entrainment in a consistent manner and does not produce any unphysical numerical entrainment. Finally, we would like to note that the modification of the turbulent length-scale is only of minor importance with respect to the overall characteristics of the full scheme.

Results of this revised model are displayed in Fig. 7(a), showing the time evolution of the liquid-water content. For comparison, the liquid-water field generated by LES for

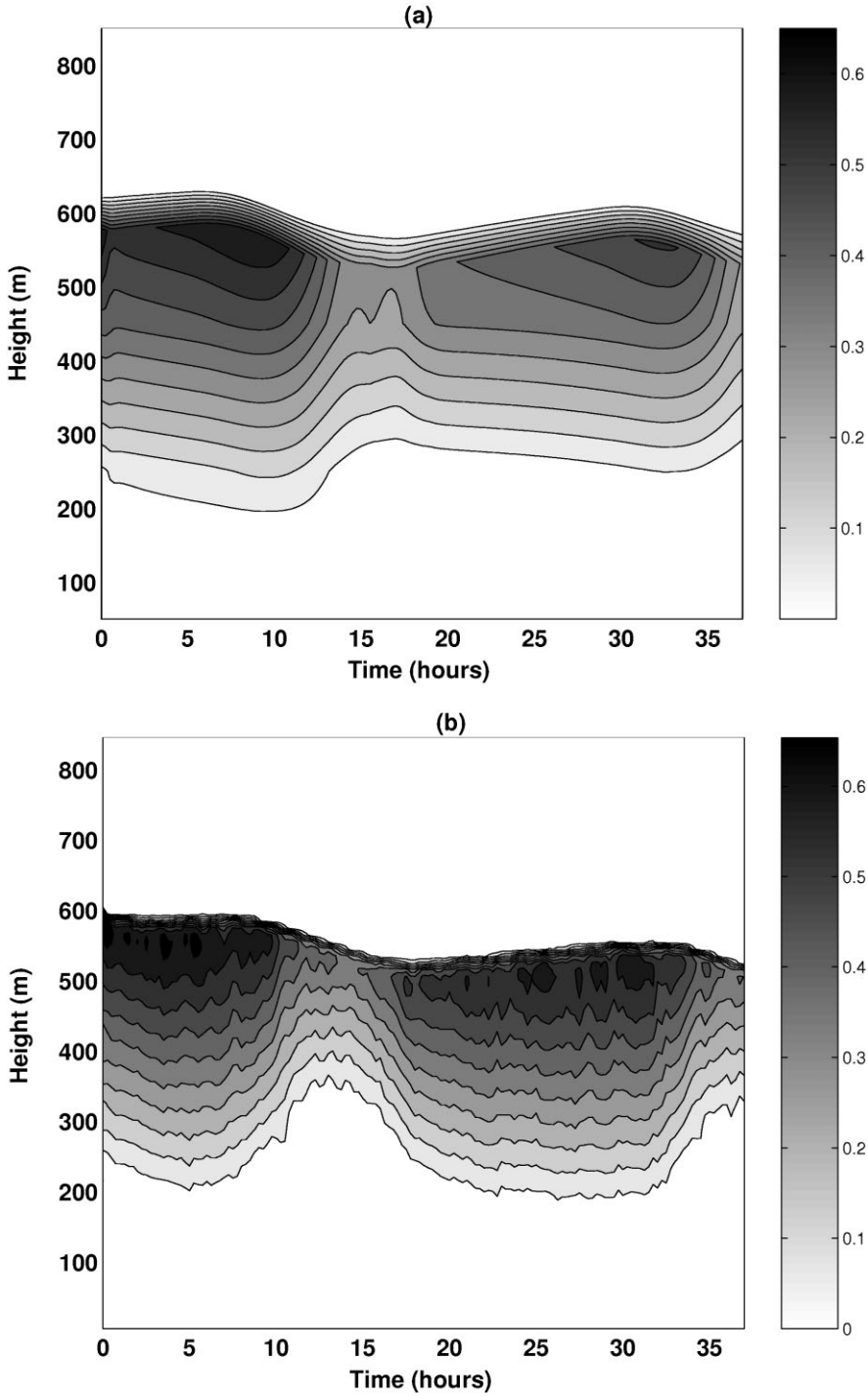

Figure 7. Time-height evolution of the liquid-water content (g kg^{-1}) for the reference case obtained using (a) the revised single-column model and (b) the large-eddy simulation model.

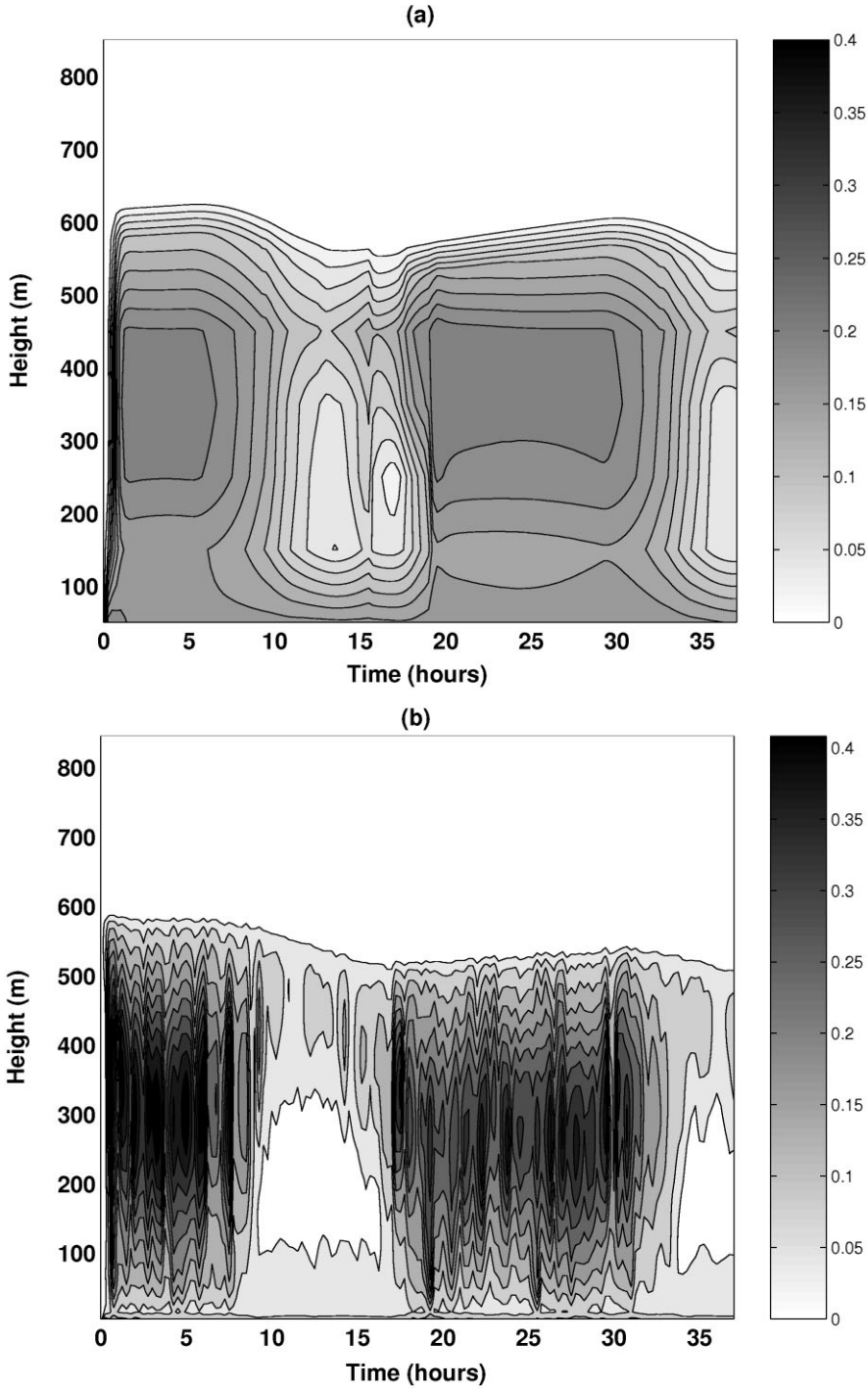

Figure 8. As Fig. 7, but showing the vertical velocity variance ($m^2 s^{-2}$).

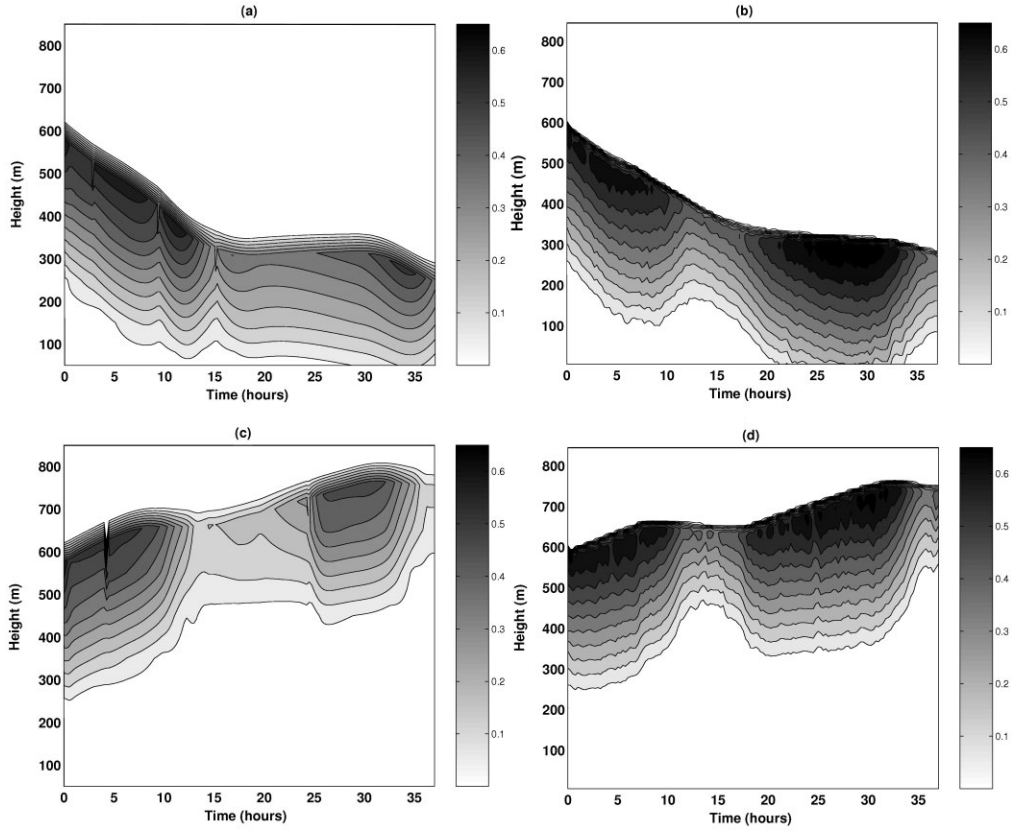

Figure 9. (a) and (b) are as Fig. 7, but for simulations where the large-scale subsidence rate was doubled. Similarly, (c) and (d) are for simulations where the large-scale subsidence rate was halved.

the same case is shown (Fig. 7(b)). For these results and in the following, time-averaged data have been used, with averaging and sampling interval of 15 minutes for both LES and SCM data. The modified SCM captures the diurnal variation of the liquid-water content profiles due to the forcing imposed by the short-wave radiation. Like the LES, the maximum cloud thickness is found during the night, and cloud deck gradually thins until the afternoon. In both models the computed liquid-water content increases with height in the cloud and reaches a maximum at $z/z_{\mathrm{i}} = 0.9$. This shows that entrainment leads to a decrease in the liquid-water content just below cloud top. A peak value in the liquid-water content of about 0.60 g kg^{-1} was predicted by both models during the night whereas during the afternoon peak values around 0.20 g kg^{-1} were produced by LES as well as by the SCM. We have also plotted in Fig. 8 the vertical velocity variance as a function of time and height for both the SCM and the LES models. Comparing those results, it is seen that the SCM produces a fair representation of the diurnal cycle, although the vertical velocity variance levels are somewhat too low, in particular in the cloud layer.

To illustrate the possibilities of the revised SCM, we conducted two additional experiments in which we used the same set-up as in the reference run, except that we doubled (halved) the large-scale subsidence rate. Figure 9 compared the time evolution of the liquid-water content as simulated by SCM and by LES for both runs. It is clearly seen that, in accord with the results of the LES, the SCM simulates a much shallower

(deeper) boundary layer in the case of a doubled (halved) large-scale subsidence rate while keeping the LWP almost constant. This is understandable because the entrainment rate should remain almost unaffected by the magnitude of the subsidence rate (see also section 4(b)). As a consequence the boundary-layer height is much lower (higher) in the run with the larger (smaller) subsidence rate. These experiments impressively demonstrate the advantage of using a front tracking algorithm in a SCM to determine the height of the entrainment layer, because the scheme does not generate numerical entrainment and hence does not keep the cloud top locked in at one level, which might occur in classical SCMs at coarse resolution.

6. Summary and conclusions

Results of numerical calculations of the diurnal cycle of the stratocumulus-topped boundary layer have been presented using the MPI LES and the ECHAM SCM. The models were initialized on the basis of observations that were collected in stratocumulus off the coast of California during FIRE I in July 1987. The LES results have been analyzed in detail and tested against the observed structure of a marine stratocumulus layer. Moreover, the performance of the standard SCM, which is taken from the ECHAM GCM, is evaluated using the LES-generated datasets. Based on this intercomparison, an improved SCM is introduced and its accuracy is assessed from a comparison against datasets built from detailed LESs. In particular, we have addressed the following items:

(1) We have studied modelling aspects of LES in the stratocumulus-topped boundary layer by focusing on some aspects of parametric and structural uncertainty. We have performed ensemble runs to give 16 realizations of the simulation. Examination of the predicted LWP and of profiles of turbulent quantities showed a non-negligible but relatively small spread among the ensemble members. Moreover, an additional run was done to test the impact of drizzle on the boundary-layer structure. We found that the primary effect of drizzle was to reduce the buoyant production of TKE, resulting in shallower boundary layers due to reduced entrainment rates. The removal of water by drizzle lowered the maximum LWP by 20%. We have also examined the sensitivity of our LES results with respect to the assumed values of various external environmental conditions. These conditions include all those environmental parameters that are needed to specify all of the mean initial and boundary conditions required to run a model simulation. The sensitivity analysis provided a framework for ranking the uncertain parameters according to their contribution to the total model variance. We found that the largest contribution to the variance of the LES-derived data products is due to the uncertainties in the cloud-top jumps of liquid-water potential temperature and total water mixing ratio and due to the net radiative forcing.

(2) A simulation performed with the standard SCM reveals that, like the observations, the SCM results show a distinct diurnal cycle in the LWP. During the night the cloud layer deepens, whereas during the day the cloud layer thins due to short-wave radiation absorption within the cloud. However, the standard SCM shows several deficiencies. In particular, results are characterized by a too low LWP and much too large values of TKE, especially near cloud top. The cause for the latter deficiency was identified and could be related to the numerical process time-splitting scheme that contains both explicit and implicit parts in which the tendencies due to radiative and diffusive processes are calculated independently. As a result, the numerical solution converges to a state that is dependent on the time step, leading to a too unstable upper-cloud

layer and to too large TKE levels. Based on these findings the SCM has been revised. The modifications include the vertical advection scheme, the numerical treatment of diffusion and radiation, and the combination of the 1.5-order turbulent closure model with an explicit entrainment closure at the boundary-layer top in combination with a front tracking/capturing method. The algorithm, is designed to provide efficient and accurate simulations of cloud-topped boundary layers given the limited vertical resolution. It is demonstrated that, with these modifications, the revised SCM provides an excellent simulation of the diurnal cycle of the stratocumulus-topped boundary layer which is significantly improved compared to the one performed with the standard SCM.

Finally, we would like to comment on the applicability of the front tracking/capturing algorithm in three dimensions. To implement the method in a 3D host numerical model, we suggest that the following procedure be performed at every time step:

(a) Map prognostic thermodynamic variables from the local inhomogeneous mesh to the fixed grid of the host model.

(b) Calculate horizontal advection of prognostic variables on the fixed grid and move the entrainment interface according to the horizontal advective process, i.e.:

$$\frac{\partial x_{k_0+1/2}}{\partial t} = -\mathbf{V}_{\mathrm{H}} \cdot \nabla x_{k_0+1/2}, \tag{16}$$

where $\mathbf{V}_{\mathrm{H}}$ denotes the horizontal velocity vector.

(c) Regrid thermodynamic variables on the local inhomogeneous mesh, taking into account that the entrainment interface has been shifted.

Whether the modifications applied to the standard SCM will bring major benefits in a full 3D climate model is subject to current research and will be described in a forthcoming paper.

Acknowledgements

The authors wish to thank H. Graßl for his useful comments and close interest in this study. This work has received financial support from the CEC contract EVK2-CT95-1999-00051 EUROCS.

References

Albrecht, B. A., Randall, D. A. and Nicholls, S. 1988 Observations of marine stratocumulus clouds during FIRE. *Bull. Am. Meteorol. Soc.*, **69,** 618–626

Bacher, A., Oberhuber, J. M. and Roeckner, E. 1998 ENSO dynamics and seasonal cycle in the tropical Pacific as simulated by the ECHAM4/OPYC3 coupled general circulation model. *Clim. Dyn.*, **14,** 431–450

Bechthold, P., Krueger, S., Lewellen, W. S., van Meijgaard, E., Moeng, C.-H., Randall, D. A., van Ulden, A. and Wang, S. 1996 Modelling of a stratocumulus-topped PBL: Intercomparison among different 1-D codes and with LES. *Bull. Am. Meteorol. Soc.*, **77,** 2033–2042

Beljaars, A. C. M. 1991 Numerical schemes for parameterizations. *Proc. ECMWF Seminar on Numerical Methods in Atmospheric Models*, Vol. 2, Reading, United Kingdom, ECMWF, 1–42

Betts, A. K. 1990 The diurnal variation of California coastal stratocumulus for two days of boundary layer soundings. *Tellus*, **42A,** 302–304

Blackadar, A. K. 1962 The vertical distribution of wind and turbulent exchange in a neutral atmosphere. *J. Geophys. Res.*, **67,** 3095–3102

Blascovic, M. R., Davies, R. and Snider, J. B. 1991 Diurnal variation of marine stratocumulus over San Nicolas Island during July 1987. *Mon. Weather Rev.*, **119,** 1469–1478

Bougeault, P. and Lacarrère, P. 1989 Parametrization of orography-induced turbulence in a mesobeta-scale model. *Mon. Weather Rev.*, **117,** 1872–1890

Chen, C. T. and Roeckner, E. 1997 Cloud simulations with the Max Planck Institute for Meteorology general circulation model ECHAM4 and comparison with observations. *J. Geophys. Res.*, **102,** 9335–9350

Chlond, A. 1992 Three-dimensional simulation of cloud street developing during a cold air outbreak. *Boundary-Layer Meteorol.*, **58,** 161–200

1994 Locally modified version of Bott's advection scheme. *Mon. Weather Rev.*, **122,** 111–125

Chlond, A. and Wolkau, A. 2000 Large-eddy simulation of a nocturnal stratocumulus-topped marine atmospheric boundary layer: An uncertainty analysis. *Boundary-Layer Meteorol.*, **95,** 31–55

Deardorff, J. W. 1980 Stratocumulus-capped mixed layers derived from a three-dimensional model. *Boundary-Layer Meteorol.*, **18,** 495–527

Duynkerke, P. G. and Teixeira, J. 2001 Comparison of the ECMWF Re-analysis with FIRE I observations: Diurnal variation of marine stratocumulus. *J. Climate*, **14,** 1466–1478

Duynkerke, P. G., Jonker, P. J., Chlond, A., van Zanten, M. C., Cuxart, J., Clark, P., Sanchez, E., Martin, G., Lenderink, G. and Teixeira, J. 1999 Intercomparison of three- and one-dimensional model simulations and aircraft observations of stratocumulus. *Boundary-Layer Meteorol.*, **14,** 1466–1478

Duynkerke, P. G., De Roode, S. R., Van Zanten, M. C., Calvo, J., Cuxart, J., Cheinet, S., Chlond, A., Grenier, H., Jonker, P. J., Köhler, M., Lenderink, G., Lewellen, D., Lappen, C.-L., Lock, A. P., Moeng, C.-H., Müller, F., Olmeda, D., Piriou, J.-M., Sánchez, E. and Sednev, I. 2004 Observations and numerical simulations of the diurnal cycle of the EUROCS stratocumulus case. *Q. J. R. Meteorol. Soc.*, **130,** 3269–3296

Ghan, S. J., Leung, L. R., Easter, R. C. and Abdul-Razzak, H. 1997 Prediction of cloud droplet number in a general circulation model. *J. Geophys. Res.*, **102,** 21777–21794

Grenier, H. and Bretherton, C. S. 2001 A moist PBL parametrization for large-scale models and its application to subtropical cloud-topped marine boundary layers. *Mon. Weather Rev.*, **129,** 357–377

Hignett, P. 1991 Observations of the diurnal variation in a cloud-capped marine boundary layer. *J. Atmos. Sci.*, **48,** 1474–1482

IPCC 2001 Climate change 2001: The Scientific Basis. Third assessment report of the Intergovernmental Panel on climate change. Eds. J. T. Houghton, Y. Ding, D. J. Griggs, M. Noguer, P. J. van der Linden, X. Dai, K. Marshall and S. A. Johnson. Cambridge University Press, Cambridge and New York.

Jacob, C. 1999 Cloud cover in the ECMWF reanalysis. *J. Climate*, **12,** 947–959

Klein, S. A. and Hartmann, D. L. 1993 The seasonal cycle of stratiform clouds. *J. Climate*, **6,** 1587–1606

Khairoutdinov, M. P. and Kogan, Y. L. 1999 A large-eddy simulation model with explicit microphysics: Validation against aircraft observations of a stratocumulus-topped boundary layer. *J. Atmos. Sci.*, **56,** 2115–2131

Kogan, Y. L., Khairoutdinov, M. P., Lilly, D. K., Kogan, Z. N. and Liu, Q. 1995 Modeling stratocumulus cloud layers in a large-eddy simulation model with explicit microphysics. *J. Atmos. Sci.*, **52,** 2923–2940

Lenderink, G. and Holtslag, A. A. M. 2000 Evaluation of the kinetic energy approach for modelling turbulent fluxes in stratocumulus. *Mon. Weather Rev.*, **128,** 244–258

Lenderink, G., van Meijgaard, E. and Holtslag, A. A. M. 2001 Evaluation of the ECHAM4 cloud-turbulence scheme for stratocumulus. *Meteorologische Zeitschrift*, **9,** 41–47

Lilly, D. K. 1968 Models of cloud-topped mixed layers under a strong inversion. *Q. J. R. Meteorol. Soc.*, **94,** 292–309

Lock, A. P. 1998 The parametrization of entrainment in cloudy boundary layers. *Q. J. R. Meteorol. Soc.*, **124,** 2729–2753

2001 The numerical representation of entrainment in parameterizations of boundary layer turbulent mixing. *Mon. Weather Rev.*, **129,** 1148–1163

Lock, A. P. and MacVean, M. K. 1999 The parametrization of entrainment driven by surface heating and cloud-top cooling. *Q. J. R. Meteorol. Soc.*, **125,** 271–299

Lohmann, U. and Feichter, J. 1997 Impact of sulfate aerosols on albedo and lifetime of clouds. *J. Geophys. Res.*, **102,** 13685–13700

Lüpkes, C. 1991 *Untersuchungen zur Parametrisierung von Koagulationsprozessen niederschlagsbildender Tropfen*, Verlag Dr. Kovac, Hamburg, Germany

Manzini, E., McFarlane, N. A. and McLandress, C. 1997 Impact of the Doppler spread parameterization on the simulations of the middle atmosphere circulation using the MA/ECHAM4 general circulation model. *J. Geophys. Res.*, **102,** 25751–25752

Moeng, C.-H. 1986 Large-eddy simulation of a stratus-topped boundary layer. Part I: Structure and budgets. *J. Atmos. Sci.*, **43,** 2886–2900

Moeng, C.-H., Shen, S. and Randall, D. A. 1992 Physical processes within the nocturnal stratus-topped boundary layer. *J. Atmos. Sci.*, **49,** 2384–2401

Moeng, C.-H., Lenschow, D. H. and Randall, D. A. 1995 Numerical investigations of the roles of radiative and evaporative feedbacks in stratocumulus entrainment and breakup. *J. Atmos. Sci.*, **52,** 2869–2883

Moeng, C.-H., Wyngaard, J. C., Sullivan, P. P. and Stevens, B. 1999 Including radiative effects on an entrainment rate formula for buoyancy driven PBLs. *J. Atmos. Sci.*, **56,** 1031–1049

Moron, V., Navarra, A., Ward, M. N. and Roeckner, E. 1998 Skill and reproducibility of seasonal rainfall patterns in the Tropics in ECHAM4 GCM simulations with prescribed SST. *Clim. Dyn.*, **14,** 83–100

Nigam, S. 1997 The annual warm to cold phase transition in the eastern equatorial Pacific: Diagnosis of the role of stratus cloud-top cooling. *J. Climate*, **10,** 2447–2467

Nordeng, T. E. 1994 'Extended versions of the convective parameterization scheme at ECMWF and their impact on the mean and transient activity of the model in the topics'. ECMWF Tech. Memo 206, 41 pp. (Available from European Centre for Medium-Range Weather Forecasts, Shinfield Park, Reading RG2 9AX, UK)

Roeckner, E., Arpe, K., Bengtsson, L., Christoph, M., Claussen, M., Dümenil, L., Esch, M., Giorgetta, M., Schlese, U. and Schulzweida, U. 1996 'The atmospheric general circulation model ECHAM4: Model description and simulation of present-day climate'. Max-Planck-Institut für Meteorologie Report No. 218, Hamburg. (Available from Max Planck Institute for Meteorology, Bundesstr. 55, 20146 Hamburg, Germany)

Roeckner, E., Bäuml, G., Bonaventura, L., Brokopf, R., Esch, M., Giorgetta, M., Hagemann, S., Kirchner, I., Kornblueh, L., Manzini, E., Rhodin, A., Schlese, U., Schulzweida, U. and Tompkins, A. 2003 'The atmospheric general circulation model ECHAM5. Part I: Model description'. Max-Planck-Institut für Meteorologie Report No. 349, Hamburg. (Available from Max Planck Institute for Meteorology, Bundesstr. 53, 20146 Hamburg, Germany)

Stevens, B. 2002 Entrainment in stratocumulus-topped mixed layers. *Q. J. R. Meteorol. Soc.*, **128,** 2663–2690

Stevens, B., Cotton, W. R., Feingold, G. and Moeng, C.-H. 1998 Large-eddy simulations of strongly precipitating, shallow, stratocumulus-topped boundary layers. *J. Atmos. Sci.*, **55,** 3616–3638

Stevens, B., Lenschow, D. H., Faloona, I., Moeng, C.-H., Lilly, D. K., Blomquist, B., Vali, G., Bandy, A., Campos, T., Gerber, H., Haimov, S., Morley, B. and Thorton, D. 2003 On entrainment rates in nocturnal marine stratocumulus. *Q. J. R. Meteorol. Soc.*, **129,** 3469–3493

Stull, R. B. 1998 *An introduction to boundary layer meteorology*. Kluwer Academic Publishers, Dordrecht, the Netherlands

Tiedtke, M. 1989 A comprehensive mass flux scheme for cumulus parameterization in large-scale models. *Mon. Weather Rev.*, **117,** 1779–1800

Turton, J. D. and Nicholls, S. 1987 A study of the diurnal variation of stratocumulus using a multiple mixed layer model. *Q. J. R. Meteorol. Soc.*, **113,** 969–1009

van Zanten, M. C., Duynkerke, P. G. and Ciujpers, J. M. W. 1999 Entrainment parameterization in convective boundary layers derived from large-eddy simulations. *J. Atmos. Sci.*, **56,** 813–828

White, P. W. (Ed.) 2000 'IFS Documentation Cycle CY21&4, Part IV: Physical processes'. Chapter 3, pp. 39–41. ECMWF, Reading, UK

Zhong, X., Hou, T. Y. and LeFloch, P. G. 1996 Computational methods for propagating phase boundaries. *J. Comput. Phys.*, **124,** 192–216